Journal Of Geophysical Research, Solid Earth

Supporting Information for

Subducted Oceanic Relief Locks the Shallow Megathrust in Central Ecuador

Jean-Yves Collot[1, 2, 3], Eddy Sanclemente[1, 4], Jean-Mathieu Nocquet[1, 2], Angélique Leprêtre[1], Alessandra Ribodetti[1], Paul Jarrin[2], Mohamed Chlieh[1], David Graindorge[5] and Philippe Charvis[1]

[1] Université Côte d'Azur, IRD, CNRS, OCA, Géoazur, Sophia-Antipolis, 250 rue A. Einstein, 06560 Valbonne, France, [2] Instituto Geofísico, Escuela Politécnica Nacional, Ladrón de Guevara E11-253, Ap. 2759, Quito, Ecuador, [3] Investigator of the Prometeo Project of the Ministry of Higher Education, Science, Technology and Innovation of the Republic of Ecuador,[4] Escuela Superior Politécnica del Litoral, Guayaquil, Ecuador, [5] Université de Bretagne Occidentale, Laboratoire Domaines Océaniques, Place Copernic, 29280 Plouzane, France.

Contents of this file

Introduction

This supporting information provides explanations for Multichannel Seismic Reflection processing, Pre-stack-depth-migration, accuracy and precision of depth migrated images, as well as for the inversion of Interseismic Coupling Methods and Resolution Analysis.

Text S1 - MCS processing and Pre Stack Depth Migration

MCS data was preprocessed using the Geovecteur software to prepare data for Pre-stack Depth Migration (PSDM), preserving the amplitude of the data. Preprocessing

included sorting of data to 6.25-m Common Depth Point (CDP), first pass velocity analysis, amplitudes attenuation (0.001 factor) of noisy traces, a band pass filter (4, 12, 28, 33 Hz), minimum phase operator, multiple attenuation in the frequency–wave number (FK) domain, normal move out velocity analysis, loose external mute, spherical divergence correction, predictive deconvolution, second multiple attenuation using Radon transform, inverse spherical divergence correction and inverse NMO correction, second band pass filter (3, 6, 50, 60 Hz), and sorting of CDP to shot gather. These data were then processed through Pre-stack Depth Migration (PSDM) (Thierry et al., 1999) including an iterative correction of the velocity macro-model (i.e. Migration Velocity Analysis - MVA) (Al-Yahya, 1989; Agudelo et al., 2005).

Velocity estimations based on Migration velocity analysis (MVA) are poorly constrained for depths greater than the maximum offset of the streamer (4.5 km for the SISTEUR data) (Lines, 1994; Ross, 1994). To improve the PSDM images of the reflectors located at larger depths ($z > 4.5$ km), we build a composite velocity model by mixing the velocity model inferred from PSDM plus MVA with that inferred from the first-arrival refraction and reflection travel time tomography (Gailler et al., 2007; Agudelo et al., 2009). The resultant mixed velocity model is composed of three Vp zones: (1) the shallow Vp zone extends down to a 3 km depth, and is controlled by the MCS Vp model. (2) A transition zone located between 3 and 5 km depths was created by applying a weighted average between the MCS and the WAS velocity models to avoid a sharp discontinuity between the shallow and deep zones of the mixed model. (3) The deep Vp zone extends down to 15 km, and is controlled by the WAS Vp tomography model. The mixed velocity model was used as velocity macro velocity model for PSDM of MCS data. Figures S1 and S2 show the PSDM processed Line SIS05 and SIS09. An interpreted version is shown in Figures 2 and 3 of the main text.

Text S2 - Accuracy and Precision of depth migrated images

The accuracy of the depth of the inter-plate fault “De” in Figures 2 and 3 in the main text is a key point to our interpretation and conclusions. Accurate seismic velocity model plays a central role in PSDM of seismic data since it controls the quality of the stacking of the redundant information provided by multifold data set, and the depth

accuracy of the reflectors. Lines SIS05 and SIS09, which cross each other, represent two independent data sets acquired with the same seismic sources and receivers, and processed separately with an identical processing sequence.

Quality control and the accuracy of the migrated images can be analyzed using Common Image Gathers (CIG) analysis. CIGs (or IsoX) panels represent the seismic traces sorted by diffraction angle and extracted from each partial seismic image at a given x coordinate along the profile (Figure S3). A partial image is a collection of diffracting points, which are illuminated under different angles. A continuous reflector is treated as a line of diffracting points, and the stack of all diffracting points over all angles forms the reflector image [*Thierry et al.*, 1999]. Inaccuracies of the velocity macromodel used for PSDM migration tend to curve the reflector on CIGs. When the background velocity model is overestimated, CIG reflectors curve downward, and the semblance γ factor is > 1, and vice versa for an underestimated velocity model, the γ factor is < 1 [*Al-Yahya*, 1989]. The background velocity model update is carried out through semblance estimation and background model corrections ($V_{corrected}=V_{migration} / \gamma$, [*Al-Yahya*, 1989]). Indeed, the reliability of this velocity analysis depends on the angular coverage in depth provided by the geometry of the acquisition. The depth of the De is close to the length of the streamer (4.5 km), the relative continuity of reflector De, the 60-80° reflection angle coverage at a 4-5 km depth, and the flatness of the CIGs (Figure S3) allow providing reasonable constraints on the rock velocity near reflector De (Lines 1994; Ross, 1994). We can observe that semblance calculation quantifies the flatness of the CIGs and the velocity update necessary converges toward the optimal velocity model (Figure S4). As an example, when $\gamma = 0.95$ and $V_{migration}$ varies between 4600- 5400 m/s in the De region, applying equation $V_{corrected}=V_{migration}/0.95$ suggests that theoretically the velocity could be increased by a maximum of ~5% to reach the optimal model. Therefore, for lines SIS05 and SIS09, the velocity macromodel is iteratively corrected during migration until CIGs are horizontally flattened. Final semblance γ factor ranges between 0.94 -0.98, thus indicating that a correct velocity model has been reached with an uncertainty that varies spatially between 2 and 6%. When this condition is satisfied, CIG are stacked to get the final migrated image. The correction process was stopped when the CIG were flattened, a result that also coincided with De reflectors reaching an equal depth at the cross point

between profiles SIS05 and SIS09. Figure S4 presents examples of final CIGs for SIS05 and SIS09 lines in the region where they cross each other. To analyze the depth precision for the inter-plate fault (De) in the crossing zone, the semblances γ factors are estimated. When $\gamma<1$, the migration velocity is too slow then the reflector appears too shallow. The error in depth can be estimated using the following formula: Z_corr= sqrt (1-(γ^2 -1) tang (θ_max_ mig /2)* tang (θ_max _ mig /2))*Z_mig/γ, where θ_ max_ mig is the maximum diffraction angle estimated at the depth of the reflector of interest. The horizontal axis of the CIG panel shows that θ_max_ mig is ~ 80° for line SIS05, and 60° for line SIS09. Z_corr is the correct value of the reflector depth and Z_mig is its depth value on the migrated image. In the crossing region of both lines, Z_mig is 4.85-5.0 km on SIS05 and 4.85-4.9 km on SIS09 (Figure S4). For reflector De at X=30 km along line SIS05, the calculated depth error between Z_corr and Z_mig is +0.3 km meaning that the correct depth for reflector De could be 0.3 km deeper. The depth-percentage error for reflector De at X=30 km on line SIS05 is 0.3/4.9*100, about 6% of the reflector depth. The depth error of reflector De at X=50 km on line SIS09 is 0.1/4.9*100, that is about 2% of the reflector depth. In this case, Z_mig depth of the inter-plate fault is close to 4.9 km on both sections. We consider that at the intersection between the lines, the depth precision on De reflector is < 6%, i.e. <300 m.

Text S3 - ***Inversion of Inter-seismic Coupling Method***

We use the virtual back-slip approach (Savage, 1983) and calculate the Green's functions relating the unit slip at a given subfault to the east, north and up components at GPS sites for an homogeneous semi-infinite elastic half-space (Okada, 1992) using a fixed rake consistent with the Nazca plate/North Andean Sliver motion as defined in Nocquet et al. (2014). Our inversion strategy follows the linear Bayesian approach for the Gaussian case proposed by Tarantola, (2005), which minimizes a cost function:

$$S(m) = \frac{1}{2}\left[(Gm-d)^t C_d^{-1}(Gm-d) + (m-m_0)^t C_m^{-1}(m-m_0)\right] \quad (1)$$

where m is the vector of back-slip amount in each subfault, m_0 is an a priori model for coupling distribution, d is the vector of observations including the GPS

123 velocity components. G is the model matrix including each individual subfault back-slip
124 contribution to d. C_d and C_m are the variance-covariance matrices associated with the data
125 and the a priori model respectively. C_d is taken as a diagonal matrix including the
126 standard deviation derived from the geodetic analysis. C_m is an exponential matrix of the
127 form:

$$C_m(i,j) = \sigma_m^2 \exp\left(-\frac{d(i,j)}{L}\right) \quad (2)$$

128

129 where d(i, j) is the distance between two subfaults j, and I L is the critical distance
130 of correlation for slip. The cost function is minimized using the bounded least-squares
131 algorithm from Stark & Parker (1995) with bounds for m in the interval [0 ; ν_{plate}], where
132 ν_{plate} is the Nazca plate / North Andean Sliver velocity.

133 **Text S4 -** ***Interseismic Coupling Inversion Resolution Analysis***
134

135 In order to first get a sense of the ability of GPS data to recover coupling at depth,
136 Figure S6 shows the sum displacements at the GPS sites induced by a unit slip at each
137 individual subfault (resolution power, Loveless and Meade, 2011). Figure S6a indicates
138 that small changes in coupling at sites ISPT, MLEC, SLGO generate relatively large
139 displacements at GPS sites and coupling at this area is expected to be well constrained.
140 Figure S6b shows the formal error (1-σ confidence level), derived from the square root of
141 the diagonal elements from the a posteriori covariance matrix $C_{post} = C_m - C_m G^t$
142 $(GC_mG^t+C_d)^{-1} G C_m$ (Tarantola, 2005) for a model with σ_m=4 mm/yr and L=30 km.
143 Although formal errors might underestimate the true accuracy of the inversion, Figure
144 S6b suggests that ISC is determined at the 10% level at the coast and near LPI with
145 increasing uncertainties close to the trench and southwest of LPI. Figure S6c shows the
146 diagonal of the resolution matrix defined by $R = C_m G^t (GC_mG^t+C_d)^{-1} G$. R is expected to
147 be close from the identity matrix for well-resolved parameters. Here, we used a fine
148 discretization (triangles with 4 km long edges), avoiding imposing a priori constant slip
149 over large areas of the interface, but leading to a large number of parameters to be
150 estimated. As stated by Radiguet et al. (2012), the resolution on a single parameter is low
151 (a few percent here, Figure S6c) and a better indicator is the restitution index obtained by

summing the elements of R along rows. The restitution index indicates how slip of a given subfault is retrieved by being distributed on the others subfaults. Figure S6d illustrates a good ability of the inversion to retrieve slip in most part of the interface. Specifically, ISC as close as ~15 km from the trench can be retrieved in front of LPI. Along strike, a good resolution (restitution index > 0.5) is found from the coast to ~30 km and ~40 km landward from the trench, north and south of LPI respectively.

Rather than providing just our "best" model, the chosen inversion formalism also offers the advantage to explore a range of possible models by varying 3 parameters only: the a priori model m_0, σ_m and L (Figure 8 and S7). L controls the smoothness of the solution, σ_m the weight given to smoothing and damping with respect to the a priori model m_0. Within this approach, the slip on subfaults that is not resolved by the data tends to follow the a priori model m_0. Thus, possible models with maximum (resp. minimum) coupling will be obtained for an a priori model taken as a fully coupled (resp. fully uncoupled) subduction ($m_0 = \nu_{plate}$, resp. $m_0 = 0$) and a relatively small damping factor σ_m (σ_m <5mm/yr). The range of acceptable models is fixed to a conventional value of $\chi 2 = 330$, corresponding to a confidence level of 80% for a model to fit the GPS data. Because our study is concerned with the shallowest part of the subduction around the location of the seamount, the $\chi 2$ statistics has been calculated using the 7 CGPS sites that have the major weight on the results in the LPI area (Figure S5). Among the explored models, weaker regularization constraints provide better fit to the data for rougher models. We use an L-curve criterion (Hansen & O'Leary, 1993) to discard too rough models. More precisely, for each model, we use the Laplacian of the inverted slip to define a roughness value. We then obtain a L-curve for each m_0 and L or m_0 and σ_m. We choose the inflexion point of the obtained L-curve to exclude model rougher than the roughness of the inflexion point. The obtained L-curves are shown in Figure S7. Based on the two criterions ($\chi 2$ and L-curve), we obtain a set of acceptable models (Figure S7 and Figure 8). The minimum and maximum values from all acceptable models are then used to define the confidence interval of the coupling coefficient at each subfault, illustrated in Figure S8. The confidence intervals for the ISC shown in Figure 3 and 7b in the main text are the minimum and maximum along the seismic profiles derived from Figure S8. Figure 8 in the main text shows a selection of 6 models illustrating the range

of models fitting the data according to different values for m_0, σ_m and L. Finally, because some readers might prefer it, we also show a classical checkerboard inversion in the LPI area (Figure S9).

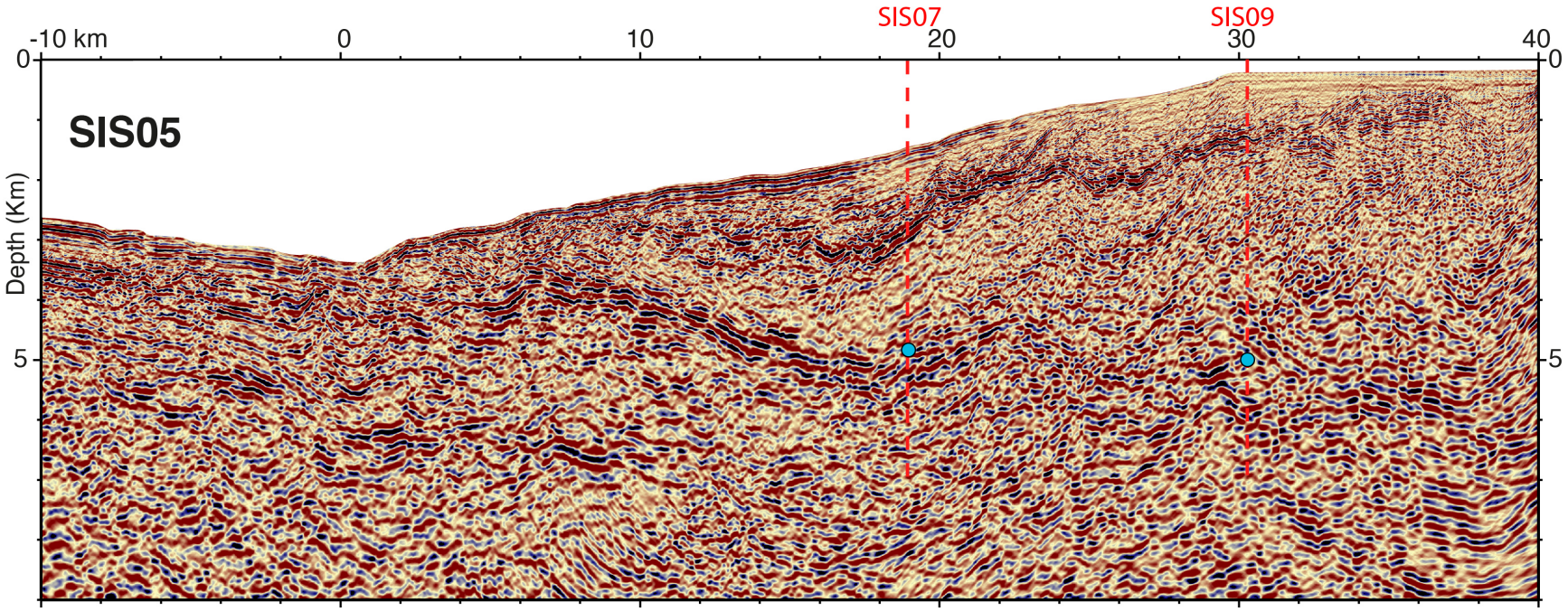

Figure S1: Prestack depth-migrated MCS line SIS05; Vertical Exaggeration = 2.0; blue dot= interpreted plate interface De at crossing MCS lines.

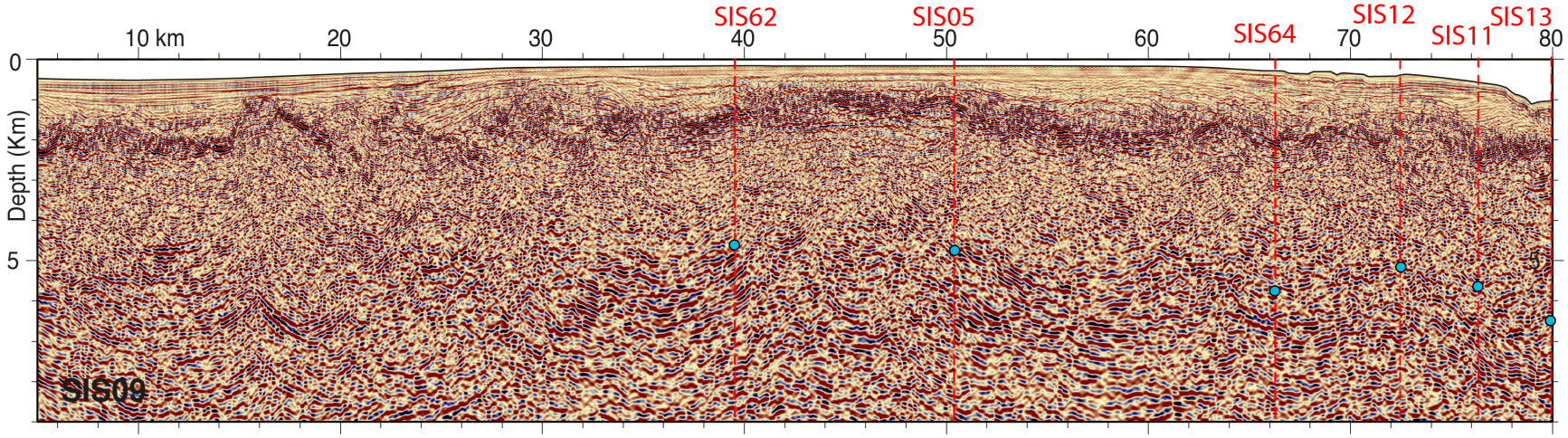

Figure S2 : Prestack depth-migrated MCS line SIS09. Vertical Exaggeration = 2.0; blue dots is plate interface "De" from crossing MCS lines indicated in red.

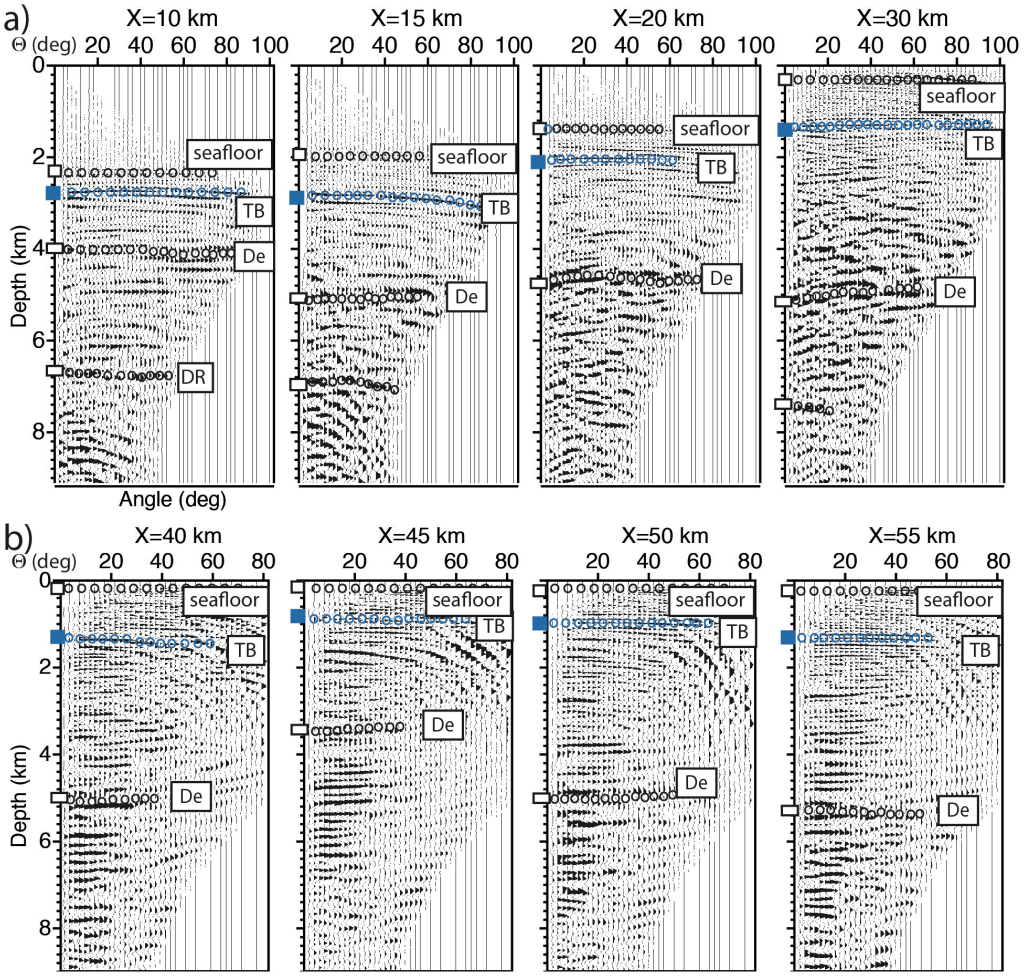

Figure S3. IsoX panels (CIGs) obtained with the mixed velocity model. (a) extracted at X=10, 15, 20, 30 km along line SIS-05 and (b) at X=40, 45, 50, 55 km along line SIS09. The horizontal axis of the CIG is the diffraction angle Θ. Sub-horizontal dotted lines plotted on the panels indicate the main reflectors, TB: Top of basement, De: Inter-plate fault, DR: Deep reflectors, according to Figures 2 and 3. Note that IsoX are quite flat and coherent, indicating that the corresponding seismic reflectors are confidently imaged. Reflector De lies at an equal depth on CIG panels located at the intersection between line SIS05 (X=30 km) and line SIS09 (X=50km).

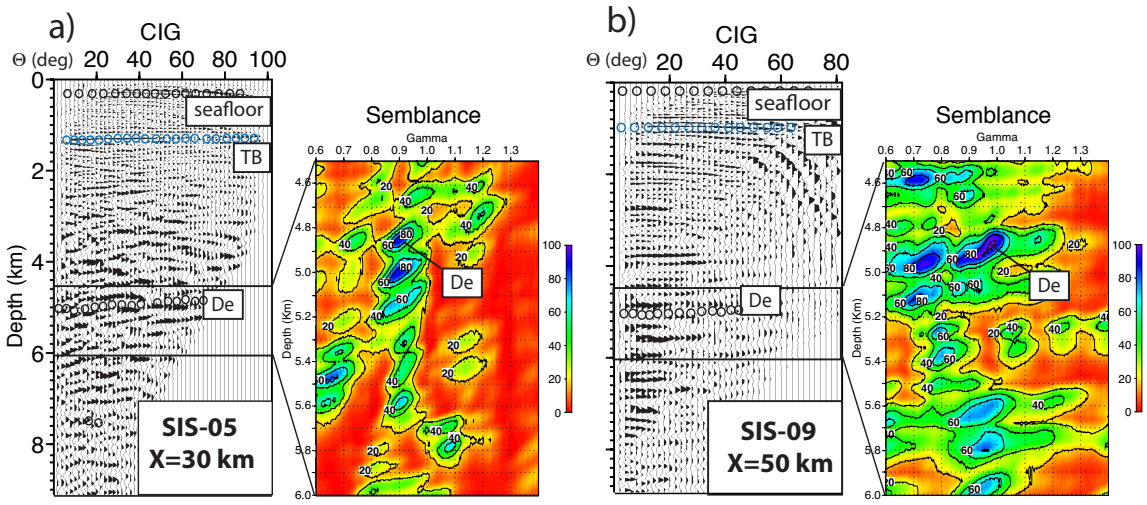

Figure S4. IsoX panels and semblance (γ factor) panels plotted between 4.5-6.0 km depth at the intersection between lines SIS05 (X=30 km) and SIS09 (X=50 km). Inter-plate fault De is characterized by the maximum energy (γ) on the semblance panels (see color scale). a) SIS-05: Maximum γ value is 0.92-0.93 at a depth of 4.8-4.9 km; b) SIS-09: Maximum γ value is 0.98-0.99 at a depth of 4.85-4.9 km.

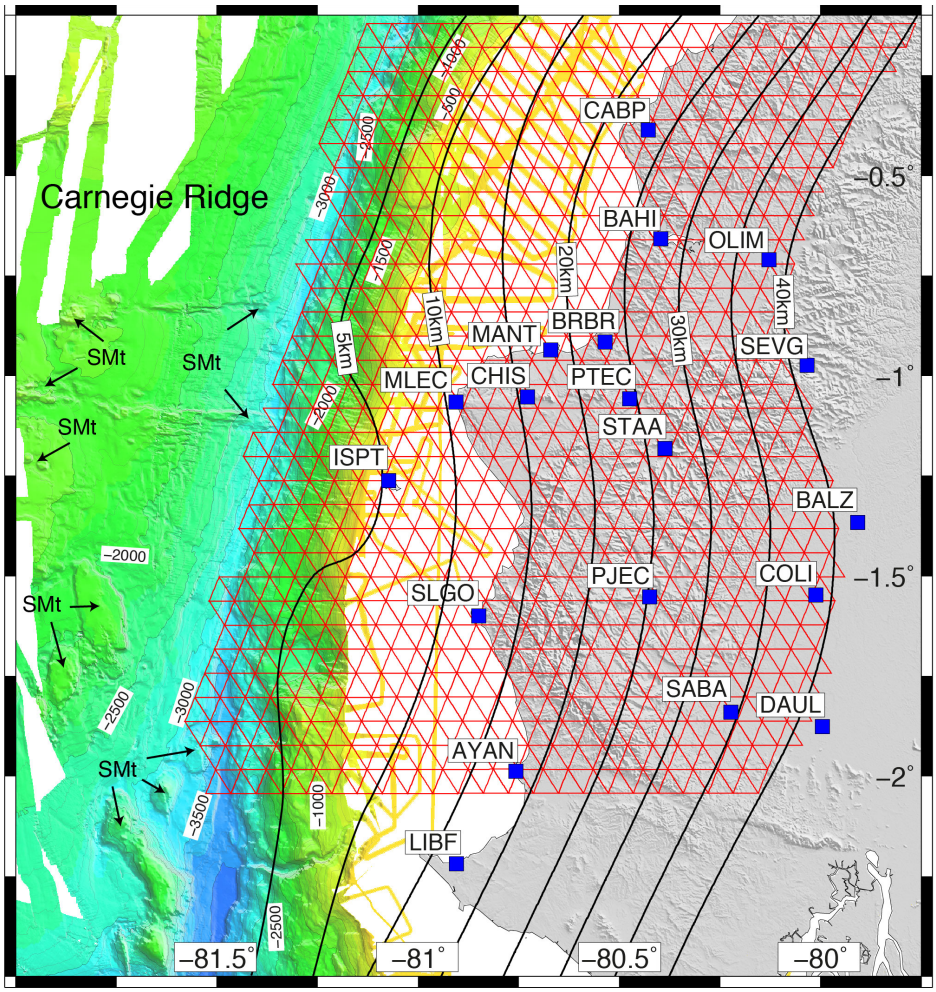

Figure S5. Carnegie Ridge Bathymetry, GPS sites and fault discretization. Bathymetric contours interval is 100 m. SMt are seamounts and ridges; Blue squares indicate GPS sites and names. Bold black lines are isodepth contours for the subduction interface every 5 km. Red triangles indicate the subfaults used for the ISC inversion.

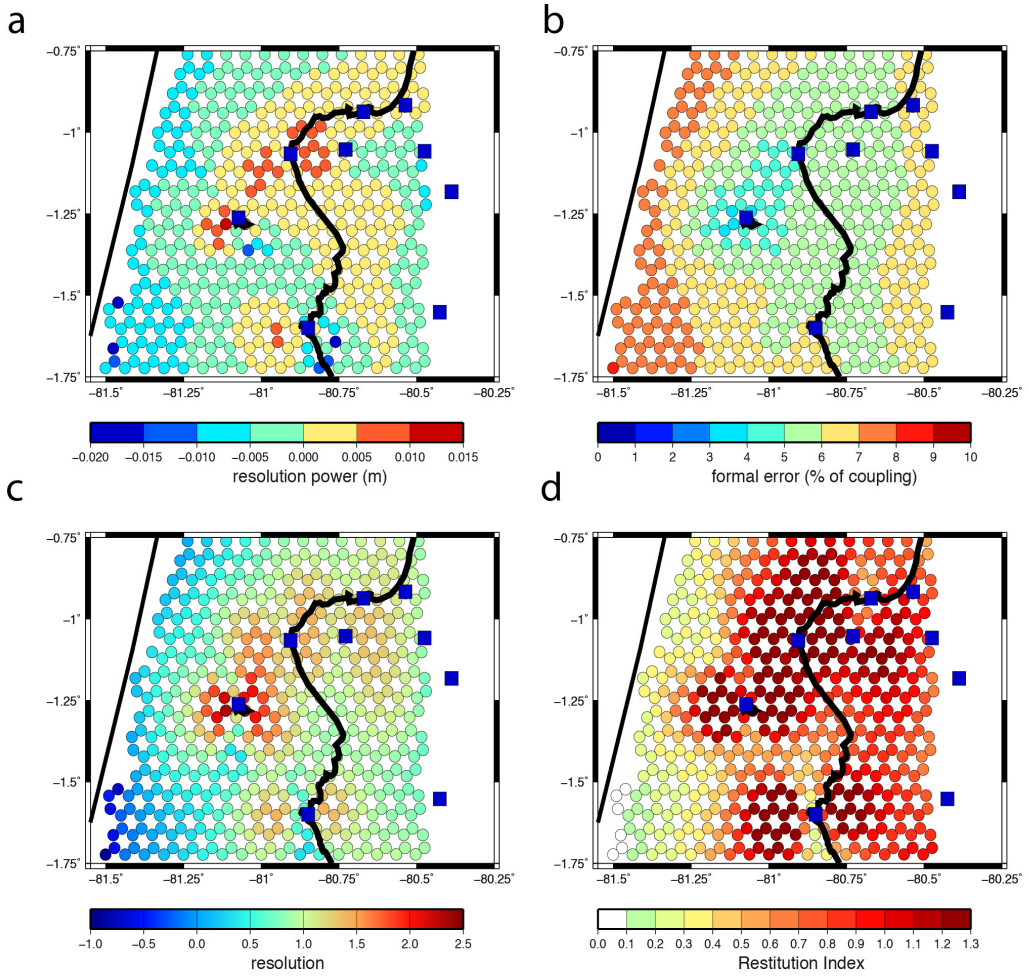

Figure S6. Resolution of ISC inversion from GPS data. (a) Power of GPS sites to constrain the slip amount at the plate interface. Color-coded values are the log10 of the sum of displacement predicted at the GPS sites for a unit slip in the convergence direction. (b) Formal errors obtained for an inversion with σm=4 mm/yr and L=30 km. Formal errors are expressed in percentage of coupling with dividing the formal error expressed in mm/yr by the plate convergence rate (47.5 mm/yr). (c) Diagonal of the resolution matrix. The color scale is log10 (resolution)+3, meaning that the highest values in the figure (~2.6) correspond to actual resolution values of ~0.4(d) restitution index.

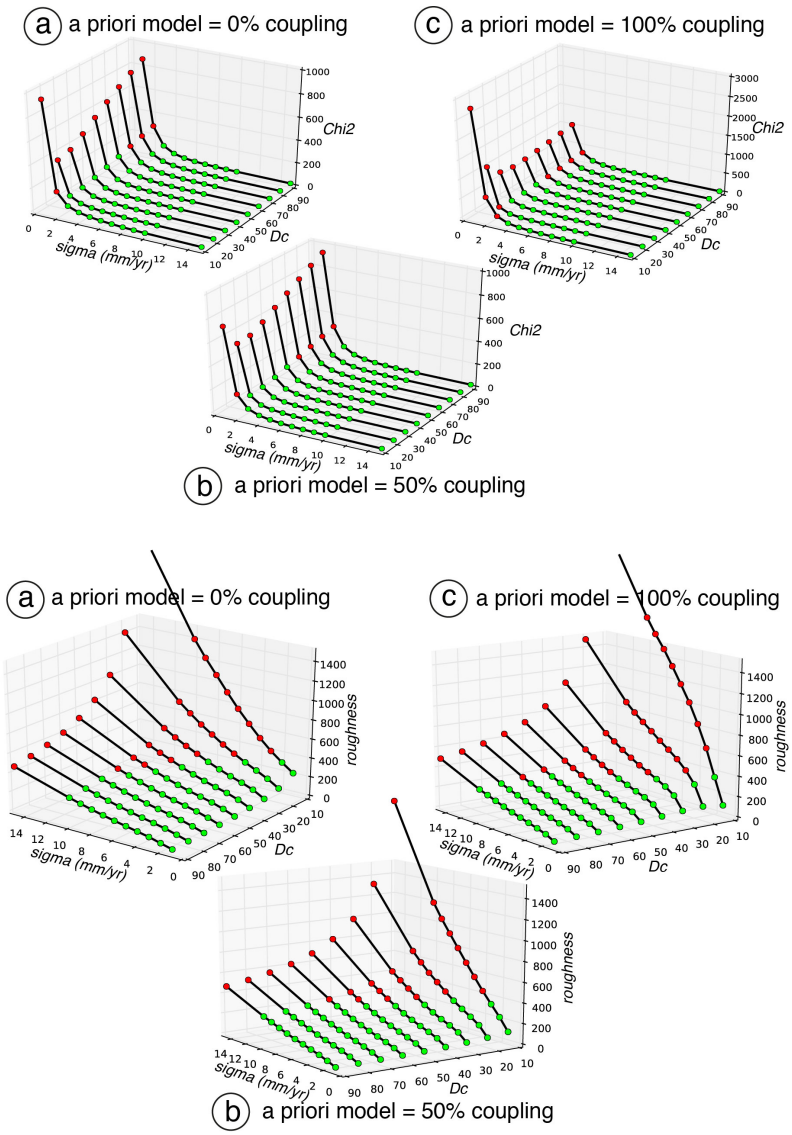

Figure S7. Misfit and roughness for the explored ISC models; Top: Chi-square as a function of the regularization parameters σ_m, L and m_0. a, b, c subplots show the results for an priori model m_0 of 0%, 50%, and 100% coupled interface. The red dots show rejected models according to the chi-square statistics calculated from the 7 GPS sites in the LPI area having significant signal at a confidence level of 80%. Green dots show models passing the same chi-square test. Bottom: Roughness as a function of the regularization parameters σ_m, L and m_0. a, b, c subplots show the results for an priori model m_0 of 0%, 50%, and 100% coupled interface. The red dots show rejected models according to the L-curve criterion. Green dots show accepted models.

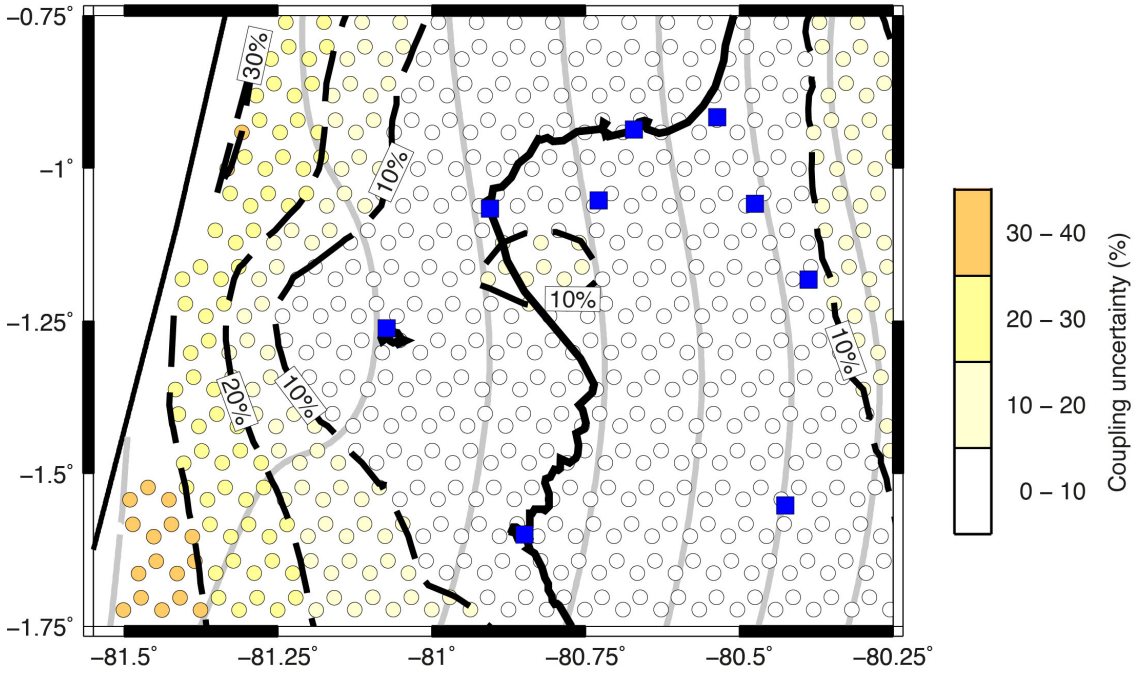

Figure S8. Coupling uncertainty in the LPI area; the coupling uncertainty map shows the difference between the maximum value and the minimum value of coupling for all selected models according to the criterion described in the text.

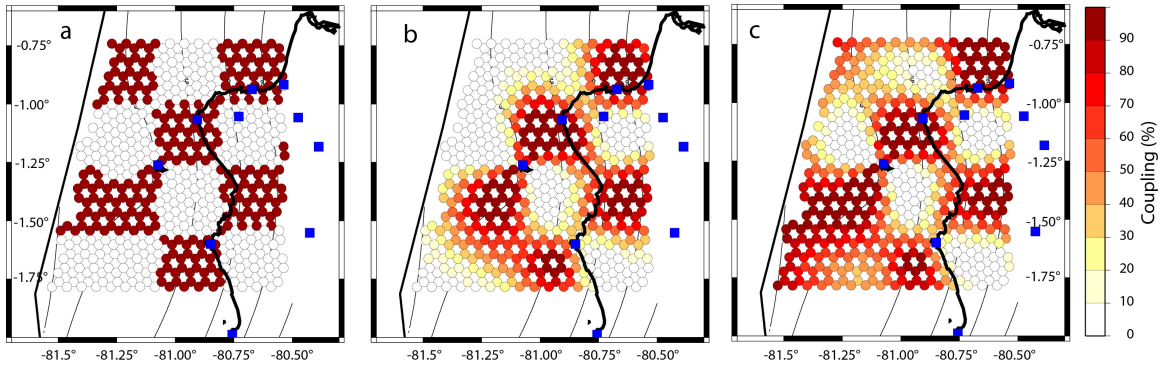

Figure S9. Checkerboard test in the LPI area; (a) Input synthetic model; locked patch are square of 30x30km; (b) Result of the inversion using an a priori model m_0=0%; (c) Result of the inversion using an a priori model m_0=100%. Blue dots indicate location of GPS sites.